Kovove Mater. 63 2025 279–287
DOI: 10.31577/km.2025.5-6.279

Production of Fe-B compounds via the self-propagating high-temperature synthesis technique

Mehmet Bugdayci[1,2]*, Levent Oncel[3], Kagan Benzesik[4]

[1] *Chemical Engineering Department, Faculty of Engineering, Yalova University, 77200 Yalova, Turkey*
[2] *Construction Technology Department, Vocational School, Istanbul Medipol University, 34810 Istanbul, Turkey*
[3] *Metallurgical and Materials Engineering Department, Faculty of Engineering and Architecture, Sinop University, 57000 Sinop, Turkey*
[4] *Department of Metallurgical and Materials Engineering, Istanbul Technical University, Sariyer, 34469 Istanbul, Turkey*

Received 13 May 2025, received in revised form 13 November 2025, accepted 21 November 2025

Abstract

This study investigated the conditions for self-propagating high-temperature synthesis (SHS) of FeB. Hematite (Fe_2O_3) and magnetite (Fe_3O_4) powders were used as iron sources, and phases generated under varied aluminum stoichiometries were identified. The SHS reactions produced loose powder products. Significant levels of impurities were detected in both experimental sets along with the FeB compounds. XRD analysis of the SHS products revealed the presence of only Fe_2B and MgO phases. Removal of Mg-based impurities was carried out through HCl leaching at different concentrations. The targeted FeB structure was obtained as intended in the experiments. Optimal conditions were identified as a reduction of the hematite-boron oxide mixture with 110 % stoichiometric Mg and subsequent leaching in 8 M HCl.

K e y w o r d s: Fe-B compounds, FactSage, SHS, borides, composites

1. Introduction

FeB alloys, consisting of transition metal borides, have attracted increasing attention over the past decade. While FeB and FeB_2 stand out as stable phases in these compounds, unstable phases such as Fe_3B and FeB_4 are also formed. The soft ferromagnetic (Fe, Fe_3O_4, FeNi, etc.) properties of the material have made it attractive. FeB compounds exhibit superior mechanical, electrical, magnetic, and hardness characteristics compared to other ferromagnetic materials. In addition, iron boride compounds possess significantly higher magnetic saturation and Curie temperatures than other metal borides [1–8]. The material also shows a high capacity for microwave absorption. Additionally, FeB compounds are utilized in H_2 absorption systems and function as electrocatalysts in O_2 evolution reactions. The biomedical industry represents another application area for Fe-B compounds. Numerous studies in the literature have focused on the biomedical applications of Fe-B compounds [9–16]. These studies reported that the material is biocompatible for MRI use and suitable for biomedical applications due to its magnetic properties and the corrosion resistance associated with its boron content. The cytotoxicity of the material was investigated, and the effectiveness of FeB nanoparticles encapsulated in liposomes against HeLa cells was determined. In addition, iron-boron compounds have been proposed as candidate materials for alternative magnetic field (AMF) applications in cancer treatment [1, 17–21]. Wear and corrosion are the two main mechanisms that degrade material performance and cause losses; therefore, developing materials resistant to these effects is crucial. Due to these properties, iron-boron compounds have recently attracted increased attention. They also offer higher mechanical and chemical stability than Fe-Cr alloys used for similar applications. The material also exhibits moderate impact resistance. Additionally, boron-alloyed steels are recognized for their high neutron absorption capacity and excellent oxidation resistance [22–27].

*Corresponding author: e-mail address: mehmet.bugdayci@yalova.edu.tr

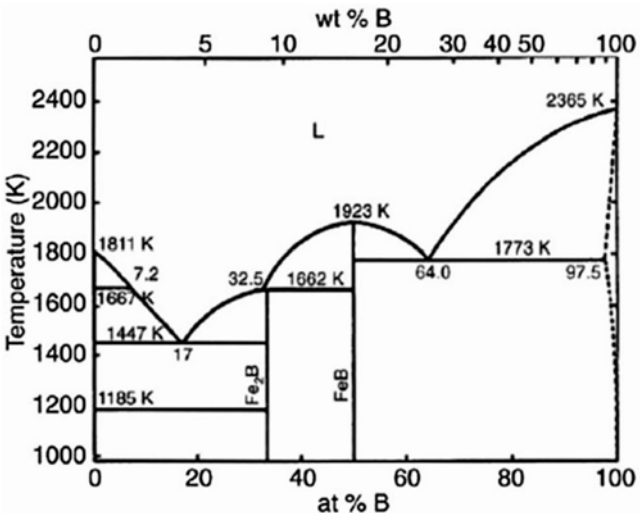

Fig. 1. Iron-boron phase diagram.

In carbon steels, boron is used as a microalloying element to enhance mechanical properties. According to the Fe-B phase diagram (Fig. 1), its solubility in the iron matrix is extremely limited. The diagram indicates that two ferroalloys, FeB and FeB_2, exist as stable phases. Their hardness values are reported in the literature as approximately 1900 HV and 1500 HV, respectively. Due to their extremely high hardness, iron-boron compounds are widely used to enhance wear resistance in boriding applications [28]. In metallurgical practice, elements with limited solubility are introduced via prealloying. For example, molybdenum (melting point 2623 ℃) does not dissolve directly in liquid steel at typical processing temperatures ($\sim$ 1565 ℃). Adding it as a ferroalloy, such as FeMo, enables the element to enter the melt more readily. The density of the components in melting processes is a critical factor affecting how alloying elements dissolve. Using ferroalloys provides a clear advantage by overcoming density-related constraints during alloying. Therefore, producing ferroalloys via alternative routes can offer clear benefits. In this study, self-propagating high-temperature synthesis (SHS) is used to produce Fe-B-based ferroalloys and to evaluate SHS as an efficient alternative production route.

Figure 1 shows the stable iron-boron phases formed by spinodal decomposition: FeB_2 with 32.5 % boron and FeB with 50 % boron. In this study, the composition of FeB – known for its superior mechanical properties – was determined as the stoichiometric ratio, and the SHS process charges were prepared accordingly. Spinodal decomposition is observed at 1650 ℃. Reaching this temperature and solidifying from the melt requires expensive equipment, long heating times, and high energy use.

By contrast, the SHS setup (variac, copper cable, resistance wire, and a crucible) sidesteps these issues: once ignited, the compact supplies the necessary heat through its own exothermic reaction, without external energy input [29].

The thermodynamic basis of this method is the Ellingham diagram of oxides. This diagram presents the ΔG values for the reactions between metals and oxygen. Accordingly, if the Gibbs free energy of the total reaction is negative, the reaction is exothermic. When the positions of the materials in the diagram are examined, it is observed that Mg, Ca, Si, and Al appear near the bottom of the diagram. Consequently, these materials are capable of reducing all other oxidized compounds. Therefore, the oxygen affinity of these materials, known as reductants, is higher than that of other elements, and when they react with oxygen, they form stable compounds, enabling the reduction of other oxides into their metallic forms [30–34].

While no direct studies have focused on the synthesis of iron-boron compounds via the SHS method, compounds such as WFeB and NdFeB have been successfully synthesized using this technique. In this study, the synthesis conditions of Fe-B compounds via the SHS method were examined, with a particular focus on the effects of different reductants (Al, Mg) and stoichiometric ratios on the production process. Furthermore, the effects of hematite (Fe_2O_3) and magnetite (Fe_3O_4) as iron sources on the synthesis process were investigated. Unwanted phases generated in the experiments using magnesium as a reductant were removed through HCl leaching, and the leaching conditions were optimized by varying the HCl molarity. Following the experiments, the products obtained from both SHS and leaching processes were characterized using XRD and SEM.

Table 1. Chemical compositions of reactant materials

Material	%Fe	%Cr	%Ni	%Zn	%Mn	%Mg	%Al	%Mo	%Si	%Ca	%Co
Fe_2O_3	Bal.	0.083	0.006	0.015	0.009	0.002	0.02	0.03	0.1	–	–
Fe_3O_4	Bal.	0.002	0.006	0.005	0.004	–	0.005	–	–	–	0.0035
B_2O_3	0.01	–	0.004	–	–	0.051	–	–	–	0.15	0.06
Al	0.028	0.24	0.04	0.56	0.45	4.65	Bal.	Rare	0.12	–	–
Mg	0.02	0.001	0.001	–	–	Bal.	2.96	–	–	–	–

Table 2. Purity and grain size of the raw materials

Raw materials	Purity (%)	Grain size
Al	> 96.0	< 150 micron
Fe_2O_3	> 99.0	< 100 micron
Mg	> 99.0	< 250 micron
Fe_3O_4	> 98.0	< 200 micron
B_2O_3	> 97.0	< 250 micron

2. Materials and method

In this study, Fe_2O_3 and Fe_3O_4 powders were employed as oxidized iron sources; B_2O_3 powder served as the boron source, and Al and Mg powders were used as reductants. Raw materials were supplied by the Nanokar company. The impurities of the materials are presented in Table 1, and the particle sizes of the raw materials are given in Table 2.

Fe-B synthesis began with an assessment of aluminothermic reduction conditions using Fe_2O_3 as the initial iron source; stoichiometric ratios followed (Eq. (1)). Subsequently, Fe_3O_4 served as the Fe source; the corresponding reaction is given in Eq. (2). The magnesiothermic reduction of Fe_2O_3 was also investigated, and its stoichiometry was determined as in Eq. (3). The codes used throughout the study to represent different mixtures, stoichiometric ratios, and synthesis methods are summarized in Table 3.

$$Fe_2O_3 + B_2O_3 + 4Al \rightarrow 2FeB + 2Al_2O_3, \quad (1)$$

$$2Fe_3O_4 + 3B_2O_3 + 11.3Al \rightarrow 6FeB + 56Al_2O_3, \quad (2)$$

$$Fe_2O_3 + B_2O_3 + 6Mg \rightarrow 2FeB + 6MgO. \quad (3)$$

As can be seen from Eqs. (1)–(3), FeB was determined as the target alloy in the study. In the aluminothermic experiments, the stoichiometric amount of Al (100 %) was determined based on Eqs. (1) and (2), after which the Al content was varied up to 115 in 5 % increments. As a result, the optimum Fe source and reductant stoichiometry were determined. In the magnesiothermic experiments, Fe_2O_3 was used as the iron source and reduced with 105 % of the stoichiometric amount of magnesium. Impurities arising from the magnesiothermic SHS experiments were removed by leaching in 6, 8, and 10 M HCl to investigate optimal conditions for impurity removal. After SHS and leaching, microstructures were examined with a Carl Zeiss Sigma 300 VP scanning electron microscope (SEM). Crystal structures were analyzed by PANalytical X'Pert^3 Powder XRD, and the patterns were processed with *X'Pert HighScore software*. For particle size analysis (PSA, Malvern^{TM} Mastersizer 2000) was used. The experimental flowchart is shown in Fig. 2.

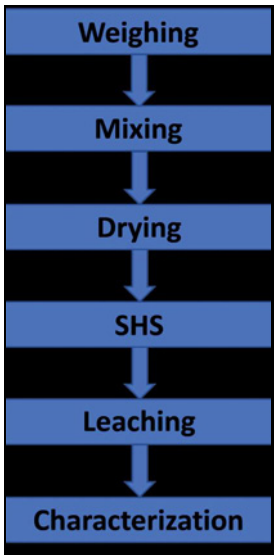

Fig. 2. Flowchart of experiments.

An identical protocol was followed during the experiments; initial weighing was conducted according to the determined stoichiometries, as illustrated in Fig. 2. Subsequently, the powder mixtures were blended in a Turbula mixer for one hour to achieve homogenization. Samples were oven-dried (ETUV) at 105 ℃ for 1 h to remove residual moisture. Subsequently, the dried mixtures were transferred into a Cu crucible, and a W wire was positioned at its upper surface to serve as a trigger. The current supplied from the variac via a copper cable was obstructed by the W wire, leading to its heating, which in turn initiated the reaction. The combustion process concluded spontaneously within approximately 15 seconds, yield-

Table 3. Sample codes and synthesis routes of the Fe-B compounds

Code	Iron Source	Reductant	Stoichiometry (%)	Method
H100-H115	Fe_2O_3	Al	100–115	Aluminothermic
M100-115	Fe_3O_4	Al	100–115	Aluminothermic
Mg110	Fe_2O_3	Mg	110	Magnesiothermic

Table 4. Detected phases and their corresponding PDF reference numbers (identified using *X'Pert HighScore software*).

Formula	Al	Fe_3BO_6	Fe_3O_4	Fe_2B
Pdf no.	00-001-1180	98-000-8068	98-006-2197	96-151-1092 03-065-2693
Formula	Al_2O_3	$FeBO_3$	MgO	FeB
Pdf No.	00-050-0741	01-076-0701	01-075-1525	01-076-0092

ing a reaction product as a loose, powdery substance. The SHS samples underwent characterization. Subsequently, the magnesiothermically reduced sample was treated with HCl at 80 ℃ for 1 hour under magnetic stirring at 450 rpm.

3. Results and discussion

In experiments aimed at developing Fe-B alloys, initial aluminothermic reductions were conducted using magnetite as the Fe source, with the aluminum stoichiometry varied at 5 % intervals. Samples were coded accordingly. Figure 3 shows the XRD analysis results of the samples obtained from the experiments. Accordingly, the M100 sample corresponds to the stoichiometric amount of Al (100 %), whereas M110 represents a composition containing 110 % of the required stoichiometric amount. Figure 3 shows that Al appears as the main peak in all mixtures. Following aluminum, ferroborate and magnetite phases are predominantly observed. The presence of significant amounts of magnetite and aluminum indicates that the reduction was not efficient. Based on this observation, magnetite and Al did not react at the expected rate. Additionally, two low-intensity peaks and the Fe_2B phase are observed. However, the dominance of ferroborates indicates that, if the reaction proceeds, the resulting phase is likely to be Fe_3BO_6. In the initial set of experiments, Fe-B alloys were not obtained efficiently. All reference codes of the detected phases obtained from XRD analyses were identified using *X'Pert HighScore software* and are collectively listed in Table 4.

In the experiments conducted for the production of Fe-B compounds, the reduction conditions of the magnetite, boron oxide, and aluminum system were first investigated. In the second stage, hematite was used as the Fe source, and the procedures applied in the first set were repeated. In this stage, the samples were labeled with H instead of M, and variations in Al stoichiometry were shown. Figure 4 presents the XRD patterns of the samples obtained from the experiments. Accordingly, Al_2O_3 and Al were predominantly detected. According to Eq. (1), the presence of the Al_2O_3 phase was expected; however, a significant amount of unreacted Al was also detected in the structure. Additionally, Fe_2B and $FeBO_3$ were detected at all mixing ratios. Among the SHS products, the 110 % stoichiometry samples (M110 and H110) showed the strongest, sharpest XRD peaks, indicating the most effective formation of Fe-B compounds. A noticeable decrease in the intensity of the formed structures was observed at 115 % stoichiometry in both sets of experiments. This is attributed to the reduction of Al_2O_3 by excess aluminum, which lowers the specific heat and consequently reduces the overall efficiency.

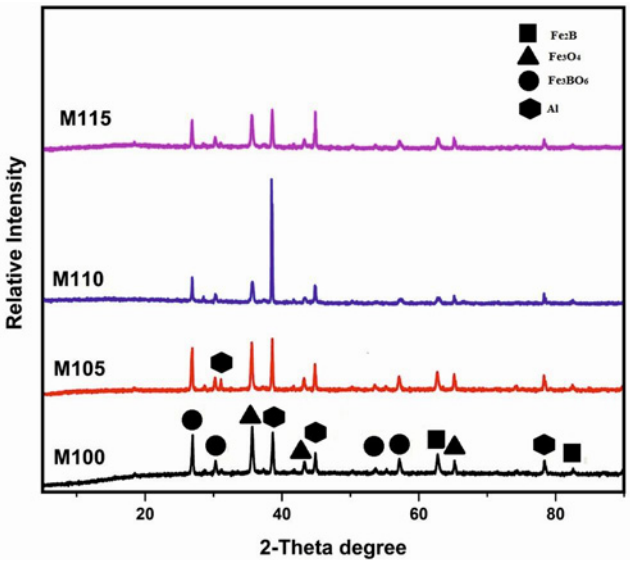

Fig. 3. XRD patterns of magnetite used in aluminothermic reduction for the synthesis of Fe-B compounds.

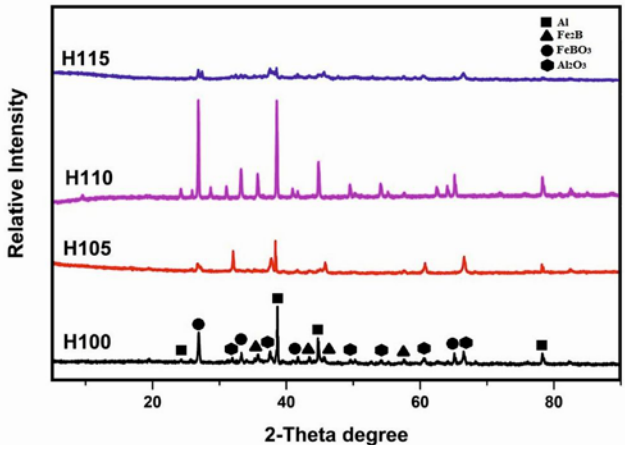

Fig. 4. XRD patterns of hematite used in the aluminothermic reduction for Fe-B compound production.

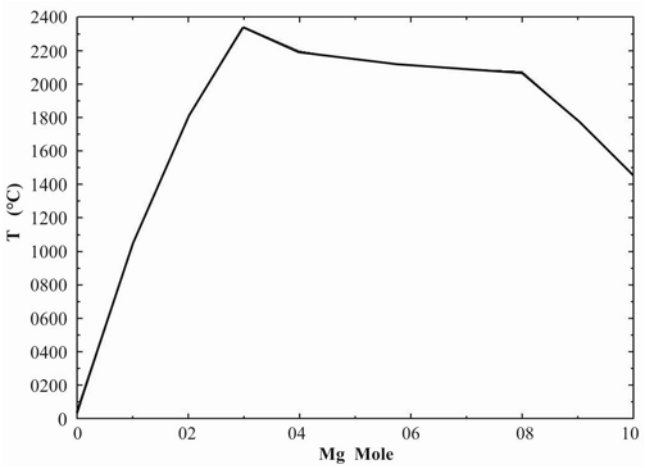

Fig. 5. Adiabatic temperature values as a function of Mg amount.

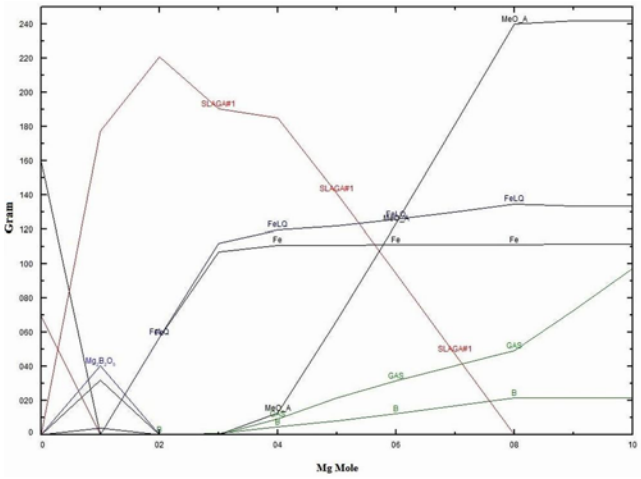

Fig. 6. Possible phases formed with increasing Mg content in the hematite–boron oxide–magnesium reduction system.

Comparison of Figs. 3 and 4 shows that the use of hematite as the Fe source resulted in a greater formation of Fe-B compounds. In both sets of experiments, the 110 % stoichiometric mixture yielded the highest amount of Fe-B compounds. Therefore, hematite was selected as the Fe source in the magnesiothermic experiment, and the reductant stoichiometry was determined to be 110 %. Thermodynamic modeling, conducted using *FactSage 7.1 software* for the magnesiothermic system before the experiments, is presented in Figs. 5 and 6. In both sets of aluminothermic experiments using different iron oxide sources, the targeted phase FeB could not be obtained; however, another stable Fe-B compound, the Fe_2B structure, could be formed.

Figure 5 illustrates the variation in adiabatic temperature with increasing amounts of Mg. In SHS processes, a minimum adiabatic temperature of 1527 ℃ is required for the initiation of the reaction. According to Fig. 5, this threshold was reached with the addition of 2 moles of Mg. When 4 moles were used, the temperature exceeded 2200 ℃ and remained above this level up to 8 moles. This indicates that, based on Eq. (3), in the system where 100 % stoichiometric Mg corresponds to 6 moles, no drop in adiabatic temperature occurs at 105 and 110 % stoichiometric levels.

In addition to the adiabatic temperature, possible phase formations were simulated using *FactSage software*, and the results are presented in Fig. 6. Magnesium borate phases were formed in significant amounts up to 2 moles but did not remain stable beyond this point. The Fe phase exhibits a high yield with an Mg input of 4 mol; the B phase attains its highest concentration when the Mg input exceeds 6 mol. This indicates that more than 6 mol of Mg is required to form Fe-B compounds. The 110 % stoichiometric Mg used here exceeds 6 mol and is therefore appropriate; at this level, both Fe and B reach their maximum concentrations. Considering the thermodynamic modeling results and data from aluminothermic experiments, hematite and boron oxide were reacted using 110 % stoichiometric Mg. Subsequently, the resulting structures were characterized by XRD, and the findings were compared with those from aluminothermic experiments using 110 % Al, as shown in Fig. 7. As a result of using magnesium as the reducing agent, the phases formed had a lower intensity compared to those observed with aluminum. The gas phase observed just above boron with increasing Mg amounts in Fig. 6 is considered the reason for this outcome. On the other hand, Fig. 7 shows that only the phases

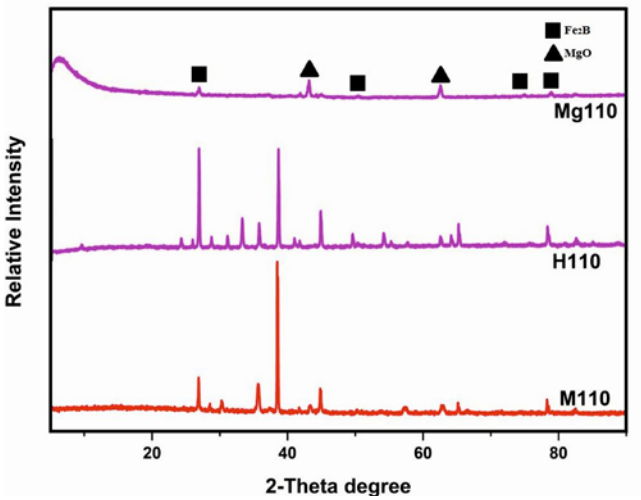

Fig. 7. XRD patterns of 110 % stoichiometric samples used in the synthesis of Fe-B compounds (Mg110: magnesiothermic sample, H110: hematite-based aluminothermic sample, M110: magnetite-based aluminothermic sample).

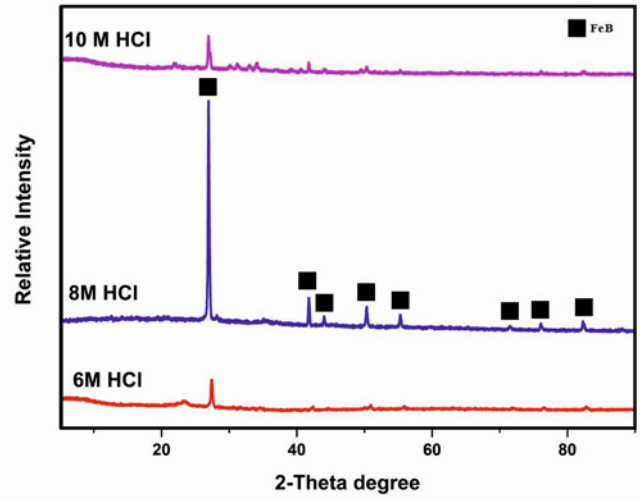

Fig. 8. XRD graphs of leached samples.

represented by the square (Fe_2B) and triangle (MgO) symbols were detected, confirming the success of the reaction according to Eq. (3). This indicates that the reaction proceeded as intended when compared to the aluminothermic experiments.

This study addressed the synthesis of Fe-B compounds. The 110 % Mg condition yielded Fe_2B along with MgO, so the product contained MgO-derived impurities. Purification toward FeB was carried out by leaching in 6, 8, and 10 M HCl. The results are presented in Fig. 8. As shown in Fig. 8, impurities were removed at all acid concentrations; however, the most intense peaks were observed in the 8 M solution. According to the XRD pattern, no phase other than FeB, which was targeted in this study, was detected. When the acid concentration reached 10 M, the FeB phase dissolved into the solution, resulting in a significant loss of the target material. Accordingly, the optimum HCl concentration was determined to be 8 M based on the leaching experiments.

After the SHS (Self-propagating High-temperature Synthesis) reaction, the product mainly consists of Fe_2B and MgO phases. The subsequent leaching process in hydrochloric acid (HCl) induces a phase transformation, which can be explained in two steps:

1. Dissolution of MgO:

$$MgO + 2HCl \rightarrow MgCl_2 + H_2OMgO + 2HCl. \quad (4)$$

In this step, MgO is completely dissolved, leaving behind the boride-containing phase.

2. Selective dissolution of Fe from Fe_2B:

Fe_2B is relatively Fe-rich compared to FeB. During leaching, hydrochloric acid selectively dissolves excess Fe atoms from the Fe_2B lattice, especially from Fe-enriched regions. Since boron is more inert to acidic

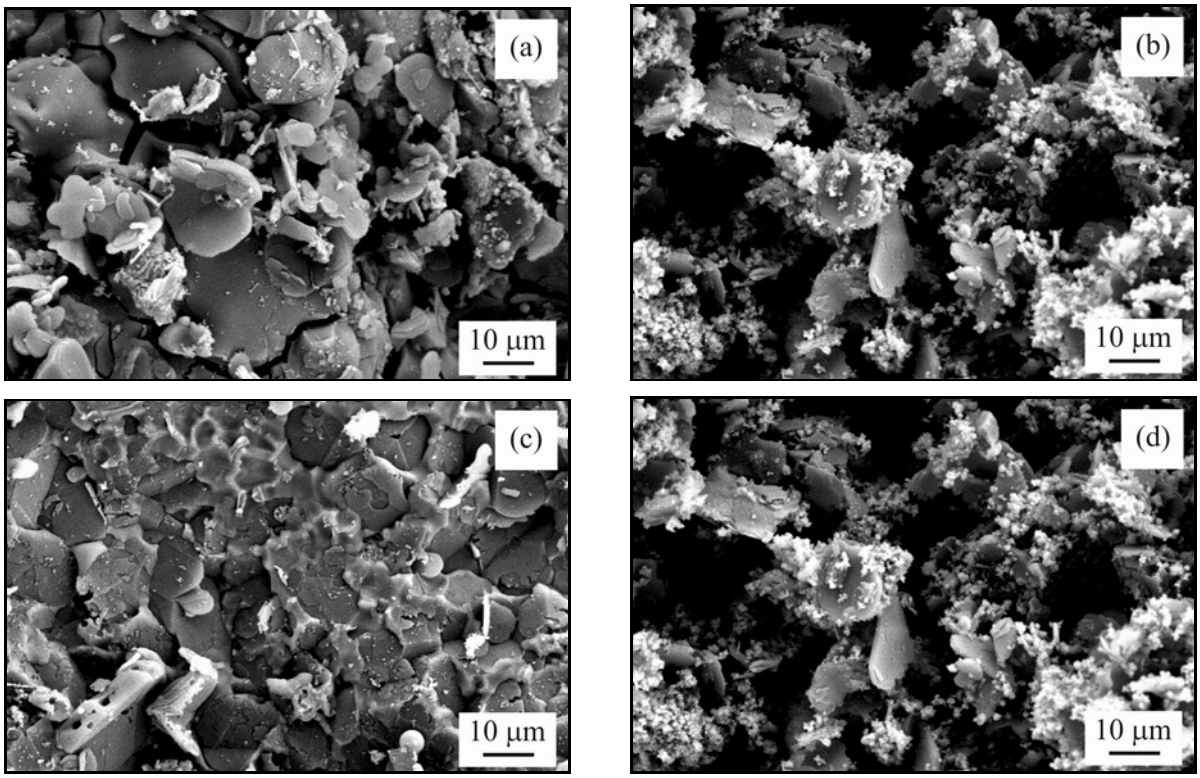

Fig. 9. SEM images of SHS-synthesized samples with 110 % stoichiometry: (a) H110, (b) M110, (c) Mg110, and (d) the sample leached with 8 M HCl.

attack, the boron-to-iron ratio in the remaining solid increases, leading to the stabilization of the FeB phase:

$$Fe_2B + 2HCl \rightarrow FeB + FeCl_2 + H_2 \uparrow . \quad (5)$$

In the overall mechanism, MgO is removed as soluble $MgCl_2$, Fe_2B undergoes partial dissolution, resulting in the loss of excess Fe, and the residual solid stabilizes as FeB, which is more boron-rich compared to Fe_2B. Thus, the phase transformation from $Fe_2B \rightarrow$ FeB during HCl leaching is driven by selective Fe dissolution and boron enrichment of the solid residue.

The stability of FeB against hydrochloric acid leaching can be attributed to its boron-rich composition and strong Fe-B bonding. While Fe_2B is relatively iron-rich and thus susceptible to selective dissolution of excess Fe atoms in acidic media, FeB possesses a more compact and chemically stable crystal structure. In addition, boron exhibits high resistance to acidic attack, and the enrichment of boron at the FeB surface may form a protective layer that passivates the phase against further dissolution. As a result, Fe_2B is transformed into FeB during leaching, whereas FeB itself remains stable under these conditions.

The SEM technique was used to characterize the microstructure of the samples. Figures 9a–d present the microstructures of SHS-synthesized samples with 110 % stoichiometry: (a) H110, (b) M110, (c) Mg110, and (d) the sample leached with 8 M HCl, identified as the optimal condition based on XRD analyses.

In the SEM analysis, a comparison of Figs. 9a,b, in line with the XRD results, revealed that composite grains formed under experimental conditions using hematite as the Fe source. In contrast, when magnetite was used, no compounds were observed, and Al structures were found to be distributed over the magnetite powders. Figure 9c shows that the reduction of hematite with magnesium resulted in a bulk structure composed of grains larger than 10 microns. As shown in Fig. 9d, after leaching with 8 M HCl, the sample was purified of impurities, and the grain size decreased to below 5 microns, resulting in a structure more favorable for the sintering process. The particle size distribution of the samples in Figs. 9c,d was performed, and the findings are presented in Fig. 10. Accordingly, the average grain size of the Mg 110 sample was calculated as 12.845 μm, and that of the sample obtained after 8M HCl leaching was 2.436 μm. These values are consistent with the SEM images. Accordingly, a significant decrease in the grain size of the powders was observed as a result of the leaching process.

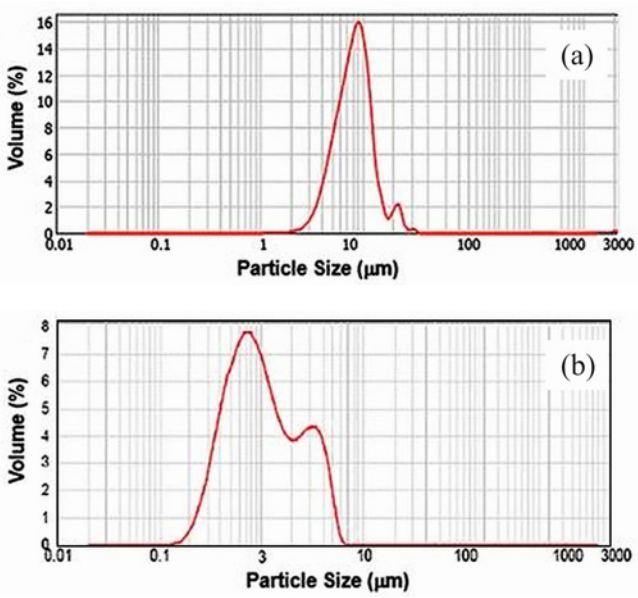

Fig. 10. Particle size distributions (a) Mg110 and (b) the sample leached with 8 M HCl.

4. Conclusions

In experiments aimed at synthesizing FeB compounds, magnetite was initially used as the Fe source, and the reduction conditions of its mixture with boron oxide, using aluminum, were investigated. Although a small amount of the Fe_2B phase was formed, the target composition was not achieved, and the structure was mainly composed of Al and Fe_3O_4. In the second stage of the experiments, as in the first set, the effect of varying aluminum stoichiometry on FeB production was investigated, using hematite as the Fe source. Although a greater amount of FeB compounds was obtained compared to the first set of experiments, the structure still contained 50 % Al and Al_2O_3 phases. In both experimental sets, the highest amount of FeB phases was observed at an Al stoichiometry of 110 %. Accordingly, the Mg stoichiometry was also set to 110 % in the design of the magnesiothermic experiments. Before the magnesiothermic experiments, the reduction system was modeled using the *FactSage thermodynamic simulation program*, and it was determined that more than 6 moles of Mg were suitable for the process based on the reaction in Eq. (3). In the third stage, the SHS process with 110 % magnesium was carried out, and XRD indicated that no phase other than Fe_2B and MgO was present. To remove MgO structures, the powders obtained after SHS were leached in 6, 8, and 10 M HCl. It was observed that high-purity FeB was obtained from the sample filtered from the 8 M HCl solution after leaching, and the intended composition was successfully achieved.

Acknowledgement

The authors thank Yalova University for supporting this study through the '2024/AP/0001' project.

References

[1] A. M. Hamayun, M. Abramchuk, H. Alnasir, M. Khan, C. Pak, S. Lenhert, L. Ghazanfari, M. Shatruk, S. Manzoor, Magnetic and magnetothermal studies of iron boride (FeB) nanoparticles, J. Magn. Magn. Mater. 451 (2018) 407–413. https://doi.org/10.1016/j.jmmm.2017.11.088

[2] L. H. Li, W. L. Wang, L. Hu, B. B. Wei, First-principle calculations of structural, elastic and thermodynamic properties of Fe-B compounds, Intermetallics 46 (2014) 211–221. https://doi.org/10.1016/j.intermet.2013.11.007

[3] Q. Liu, H. Zhao, M. Jiang, Q. Kang, W. Zhou, P. Wang, F. Zhou, Boron enhances oxygen evolution reaction activity over Ni foam-supported iron boride nanowires, J. Mater. Chem. A 8 (2020) 13638–13645. https://doi.org/10.1039/C9TA14256H

[4] P. R. Jothi, K. Yubuta, B. P. T. Fokwa, A simple, general synthetic route toward nanoscale transition metal borides, Adv. Mater. 30 (2018) 2–7. https://doi.org/10.1002/adma.201704181

[5] Y. Jiang, Y. Lu, Designing transition-metal-boride-based electrocatalysts for applications in electrochemical water splitting, Nanoscale 12 (2020) 9327–9351. https://doi.org/10.1039/D0NR01279C

[6] K. K. Zhi, Z. D. Yang, D. F. Shi, X. J. Yao, M. G. Wang, Desmodeleganine, a new alkaloid from the leaves of Desmodium elegans as a potential monoamine oxidase inhibitor, Fitoterapia 98 (2014) 160–165. https://doi.org/10.1016/j.fitote.2014.07.022

[7] X. Zhang, W. Chen, H. Luo, T. Zhou, Formation of periodic layered structure between novel Fe-Cr-B cast steel and molten aluminum, Scr. Mater. 130 (2017) 288–291. https://doi.org/10.1016/j.scriptamat.2016.12.011

[8] F. Hanguang, S. Xuding, L. Yongping, X. Jiandong, Effect of boron concentration on the corrosion resistance of cast B-bearing steel in molten zinc, Mater. Corros. 59 (2008) 948–953. https://doi.org/10.1002/maco.200805004

[9] X. Zhao, L. Li, K. Bao, P. Zhu, Q. Tao, S. Ma, B. Liu, Y. Ge, D. Li, T. Cui, Synthesis and characterization of a strong ferromagnetic and high hardness intermetallic compound Fe_2B, Phys. Chem. Chem. Phys. 22 (2020) 27425–27432. https://doi.org/10.1039/D0CP03380D

[10] X. Liu, S. Ran, J. Yu, Y. Sun, Multiscale assembly of Fe_2B porous microspheres for large magnetic losses in the gigahertz range, J. Alloys Compd. 765 (2018) 943–950. https://doi.org/10.1016/j.jallcom.2018.06.292

[11] G. Shao, J. Liang, W. Zhao, B. Zhao, W. Liu, H. Wang, B. Fan, H. Xu, H. Lu, Y. Wang, R. Zhang, Co decorated polymer-derived SiCN ceramic aerogel composites with ultrabroad microwave absorption performance, J. Alloys Compd. 813 (2020) 152007. https://doi.org/10.1016/j.jallcom.2019.152007

[12] M. Hamamci, A. A. Cerit, F. Nair, Effect of sintering parameters on the microstructure and micromechanical properties of in-situ synthesized boride phases (Fe_2B-FeB) in iron matrix composites reinforced with B_4C particles, Mater. Charact. 191 (2022) 112075. https://doi.org/10.1016/j.matchar.2022.112075

[13] A. Paksoy, S. F. Kurtoğlu, A. K. Dizaji, Z. Altintaş, S. Khoshsima, A. Uzun, Ö. Balci, Nanocrystalline cobalt-nickel-boron (metal boride) catalysts for efficient hydrogen production from the hydrolysis of sodium borohydride, Int. J. Hydrogen Energy 46 (2021) 7974–7988. https://doi.org/10.1016/j.ijhydene.2020.12.017

[14] H. Chen, X. Zou, Intermetallic borides: Structures, synthesis and applications in electrocatalysis, Inorg. Chem. Front. 7 (2020) 2248–2264. https://doi.org/10.1039/D0QI00146E

[15] S. Rades, A. Kornowski, H. Weller, B. Albert, Wet-chemical synthesis of nanoscale iron boride, XAFS analysis and crystallisation to α-FeB, J. Chem. Phys. Chem. 12 (2011) 1756–1760. https://doi.org/10.1002/cphc.201001072

[16] P. C. Verma, S. K. Mishra, Synthesis of iron boride powder by carbothermic reduction method, Mater. Today Proc. 28 (2019) 902–906. https://doi.org/10.1016/j.matpr.2019.12.321

[17] V. Torresan, A. Guadagnini, D. Badocco, P. Pastore, G. Arturo, M. Medina, M. B. F. van Raap, I. Postuma, S. Bortolussi, M. Bekić, M. Čolić, M. Gerosa, A. Busato, P. Marzola, V. Amendola, Biocompatible iron-boron nanoparticles designed for neutron capture therapy guided by magnetic resonance imaging, Adv. Healthc. Mater. 10 (2021) 1–11. https://doi.org/10.1002/adhm.202001632

[18] R. Sahara, S. Emura, S. Ii, S. Ueda, K. Tsuchiya, First-principles study of electronic structures and stability of body-centered cubic Ti-Mo alloys by special quasirandom structures, Sci. Technol. Adv. Mater. 15 (2014) 035014. https://doi.org/10.1088/1468-6996/15/3/035014

[19] H. Fatima, T. Charinpanitkul, K. S. Kim, Fundamentals to apply magnetic nanoparticles for hyperthermia therapy, Nanomaterials 11 (2021) 1–20. https://doi.org/10.3390/nano11051203

[20] A. Rajan, N. K. Sahu, Review on magnetic nanoparticle-mediated hyperthermia for cancer therapy, J Nanoparticle Res. 22 (2020) 319. https://doi.org/10.1007/s11051-020-05045-9

[21] A. Miaskowski, M. Subramanian, Specific absorption rate parameter model in magnetic hyperthermia, Proc. 2017 18th Int. Conf. Comput. Probl. Electr. Eng. CPEE 2017, pp. 27–30. ISBN 978-1-5386-1041-1

[22] X. M. Cao, R. N. Ma, J. J. Wu, M. Wen, Y. Z. Fan, A. Du, Influences of Si on corrosion of Fe-B alloy in liquid zinc, Corros. Eng. Sci. Technol. 44 (2009) 441–444. https://doi.org/10.1179/174327808X315696

[23] S. Ma, J. Xing, H. Fu, Y. He, Y. Bai, Y. Li, Y. Bai, Interface characteristics and corrosion behaviour of oriented bulk Fe_2B alloy in liquid zinc, Corros. Sci. 78 (2014) 71–80. https://doi.org/10.1016/j.corsci.2013.08.033

[24] S. Ma, J. Xing, H. Fu, D. Yi, Y. Li, J. Zhang, B. Zhu, Y. Gao, Microstructure and interface characteristics of Fe-B alloy in liquid 0.25 wt.% Al-Zn at various bath temperatures, Mater. Chem. Phys. 132 (2012) 977–986. https://doi.org/10.1016/j.matchemphys.2011.12.044

[25] S. Ma, J. Xing, H. Fu, D. Yi, X. Zhi, Y. Li, Effects of boron concentration on the corrosion resistance of Fe-B alloys immersed in 460 °C molten zinc bath, Surf. Coatings Technol. 204 (2010) 2208–2214. https://doi.org/10.1016/j.surfcoat.2009.12.010

[26] G. Liu, J. Xing, S. Ma, Y. He, H. Fu, Y. Gao, Y. Wang, Y. Wang, Effects of erosion angle on erosion properties of Fe-B alloy in flowing liquid zinc, Metall. Mater. Trans. A Phys. Metall. Mater. Sci. 46 (2015) 1900–1907. https://doi.org/10.1007/s11661-015-2820-9

[27] C. T. Zhou, J. D. Xing, B. Xiao, J. Feng, X. J. Xie, Y. H. Chen, First principles study on the structural properties and electronic structure of X_2B (X = Cr, Mn, Fe, Co, Ni, Mo and W) compounds, Comput. Mater. Sci. 44 (2009) 1056–1064. https://doi.org/10.1016/j.commatsci.2008.07.035

[28] J. Zhang, J. Liu, H. Liao, M. Zeng, S. Ma, A review on relationship between morphology of boride of Fe-B alloys and the wear/corrosion resistant properties and mechanisms, J. Mater. Res. Technol. 8 (2019) 6308–6320. https://doi.org/10.1016/j.jmrt.2019.09.004

[29] M. K. Ziatdinov, Metallurgical SHS processes as a route to industrial-scale implementation: An autoreview, Int. J. Self-Propagating High-Temperature Synth. 27 (2018) 1–13. https://doi.org/10.3103/S1061386218010132

[30] M. Bugdayci, S. Baslayici, O. Coban, F. Kaya, Self-propagating high temperature synthesis (SHS) of ZrC-TiC nanocomposites: Comparison of Mg and Al reductant usage and process optimization, J. Aust. Ceram. Soc. 60 (2024) 1541–1555. https://doi.org/10.1007/s41779-024-01062-2

[31] O. Coban, M. Bugdayci, S. Baslayici, M. E. Acma, Combustion synthesis of B_4C-TiB_2 nanocomposite powder: Effect of Mg particle size on SHS and optimization of acid leaching process, J. Superhard Mater. 45 (2023) 20–30. https://doi.org/10.3103/S1063457623010033

[32] M. Bugdayci, G. Deniz, C. Ziyreker, A. Turan, L. Oncel, Thermodynamic modeling and production of FeCo alloy from mill scale through metallothermic reduction, Eng. Sci. Technol. 23 (2020) 1259–1265. https://doi.org/10.1016/j.jestch.2020.03.003

[33] L. Oncel, Production of ferronickel from mill-scale via metallothermic process, El-Cezeri J. Sci. Eng. 7 (2020) 824–834 (in Turkish). https://doi.org/10.31202/ecjse.702804

[34] O. C. Odabas, M. Bugdayci, S. Kan, A. Turan, O. Yucel, Effects of reductant type on the combustion synthesis of NiB, Solid State Sci. 111 (2021) 106447. https://doi.org/10.1016/j.solidstatesciences.2020.106447